Icarus 272 (2016) 88–101

Contents lists available at ScienceDirect

Icarus

journal homepage: www.elsevier.com/locate/icarus

Measurements and an empirical model of the Zodiacal brightness as observed by the Solar Mass Ejection Imager (SMEI)

Andrew Buffington[a,*], Mario M. Bisi[a,b], John M. Clover[a], P. Paul Hick[a,c], Bernard V. Jackson[a], Thomas A. Kuchar[d], Stephan D. Price[d,†]

[a] Center for Astrophysics and Space Sciences, University of California, San Diego, 9500 Gilman Drive, MS 0424, La Jolla, CA 92093-0424, USA
[b] Rutherford Appleton Laboratory, RAL Space (R25-1.03), Harwell Oxford, Oxfordshire OX11 0QX, England, UK
[c] San Diego Supercomputer Center, University of California, San Diego, 9500 Gilman Drive, MS 0505, La Jolla, CA 92093-0505, USA
[d] Institute for Scientific Research, Boston College, Chestnut Hill, MA 02147, USA

ARTICLE INFO

Article history:
Received 20 October 2015
Revised 8 February 2016
Accepted 22 February 2016
Available online 2 March 2016

Keywords:
Zodiacal light
Photometry
Interplanetary dust

ABSTRACT

The Solar Mass Ejection Imager (SMEI) provided near-full-sky broadband visible-light photometric maps for 8.5 years from 2003 to 2011. At a cadence of typically 14 maps per day, these each have an angular resolution of about 0.5° and differential photometric stability of about 1% throughout this time. When individual bright stars are removed from the maps and an empirical sidereal background subtracted, the residue is dominated by the zodiacal light. This sky coverage enables the formation of an empirical zodiacal-light model for observations at 1 AU which summarizes the SMEI data. When this is subtracted, analysis of the ensemble of residual sky maps sets upper limits of typically 1% for potential secular change of the zodiacal light for each of nine chosen ecliptic sky locations. An overall long-term photometric stability of 0.25% is certified by analysis of three stable sidereal objects. Averaging the nine ecliptic results together yields a 1-σ upper limit of 0.3% for zodiacal light change over this 8.5 year period.

1. Introduction

The Solar Mass Ejection Imager (SMEI) was designed for detecting and tracking Coronal Mass Ejections (CMEs) from near the Sun to beyond the Earth, and for using that information to forecast their arrival at the Earth. Conceived as an all-sky imager (Jackson et al., 1989), SMEI viewed the outward flow of CMEs and other heliospheric structures by recording Thomson-scattered sunlight (Jackson et al., 2004; Tappin et al., 2004; Webb et al., 2006). SMEI began providing data on 5 February 2003, and was deactivated on 28 September 2011 after 8.5 years of operation (Howard et al., 2013).

SMEI was in an 840-km Sun-synchronous polar Earth orbit on board the US Air Force *Coriolis* satellite (Eyles et al., 2003; Jackson et al., 2004). The instrument consists of three baffled cameras, each viewing a $3^\circ \times 60^\circ$ strip of sky. Individual data frames were read out every four seconds for each camera. Camera 1 viewed the antisolar region and camera 3 closest to the Sun. The data frames obtained from one 102-min orbit were combined into a photometric sky map whose field of view (FOV) covered nearly the entire sky (up to ~95%). The FOV extended from as close as solar elongation $\varepsilon = 18^\circ$, to the antisolar point ($\varepsilon = 180^\circ$). SMEI's location above the atmosphere and 24-h temporal coverage provided a long time series of photometric measurements beginning in February 2003 into September 2011, interrupted only occasionally by periodic calibrations and by data outages. These data have provided three-dimensional (3-D) reconstructions of CME density and velocity (e.g., Jackson et al., 2008). In addition, SMEI observed high-altitude aurorae (Mizuno et al., 2005), searched for optical counterparts of gamma-ray bursts (Buffington et al., 2006), observed the motions of comet tails (Kuchar et al., 2008; Buffington et al., 2008), photometrically monitored stars for potential planetary transits (Spreckley and Stevens, 2007), and provided comprehensive observations of the Gegenschein (Buffington et al., 2009) using camera 1 alone.

To detect CMEs in the data, algorithms were developed to remove instrumental artifacts, individual bright stars, a residual sidereal component, and finally the zodiacal-light background. The surface-brightness of the zodiacal background is ~100× brighter than the CMEs. In and of themselves, the zodiacal maps generated in this process provide an unprecedented picture of the zodiacal dust cloud and how its geometry changes during the year as viewed from Earth.

* Corresponding author. Tel.: +1 858 534 6630; fax +1 858 534 0177.
† Deceased.
E-mail address: abuffington@ucsd.edu (A. Buffington).

http://dx.doi.org/10.1016/j.icarus.2016.02.045
0019-1035/

This article describes an empirical surface-brightness zodiacal-light model using SMEI data. The resulting representation: (1) extends the Gegenschein analysis to include measurements from camera 2; (2) makes a photometric analysis of three sidereal objects – the Andromeda Galaxy and the two Magellanic Clouds – chosen here since they are similar in brightness to the Gegenschein enhancement distribution; and finally (3) investigates potential changes at eight other sky locations. When an annually-repeating variation for each of these sky locations is removed, the respective brightnesses all remain essentially constant over the 8.5-year period. The zodiacal-light model presented here succinctly expresses average brightness as a function of day-of-year (DOY) and position in the sky.

2. SMEI data analysis and removal of stellar background

SMEI's three CCD cameras collectively viewed a $\sim$160° long $\times$ 3° wide strip of sky oriented such that its long axis lay approximately along the direction of solar elongation ε. The cameras' wavelength-dependent response was roughly triangular with a maximum at 0.7 μm linearly tapering down to zero at 0.4 μm and at 1.1 μm. The solar-spectrum-weighted mean wavelength was 0.70 μm and the full-width-at-half maximum was 0.35 μm. The point-spread function (PSF) was complex (see Fig. 8 in Eyles et al. 2003, and Fig. A3 here), and changed somewhat throughout the mission duration, which somewhat limited the effectiveness of the individual star subtraction. The PSF had an rms radius of about 0.5°. Appendix A describes the SMEI optics and PSF. Short-term differential photometric precision was 0.1% over most of the sky, but the associated photometric accuracy degraded near bright stars or the Moon, during periods of bright aurora (Mizuno et al., 2005), or when auroral electrons or South Atlantic Anomaly (SAA) protons impacted upon the CCD (Buffington et al., 2006). The present work (Section 5) certifies longer-term differential photometric accuracy to about 0.25% for the two cameras viewing farthest from the Sun. Although all three cameras are included here in constructing the zodiacal-light model, the present long-term analyses of various sky regions were restricted to data from cameras 1 and 2. Camera 3 is here omitted from these long-term analyses since it operated at an unexpectedly high temperature and suffered significantly more noise and other difficulties throughout the SMEI mission.

Data were originally recorded as per-pixel electron counts from the CCD detector that are labeled analog-to-digital units (ADUs) in our various other SMEI publications. Buffington et al. (2007) calibrated SMEI camera responses using bright stars, determined the response relationship between cameras, and (upon scaling cameras 1 and 3 to match camera 2) derived a surface brightness of one S10 (the equivalent brightness of one 10th visual-magnitude G-type star spread over one square degree: see Leinert et al., 1998; Cox 2000) in a sky map corresponding to 0.46 ± 0.02 ADUs.

Tracking apparent brightness versus time, of portions of sky along the Galactic disk, the responsivity of all three cameras diminished on average by about 1% per year. However, the bright center of the Galaxy diminished by only 0.6% per year and darker sky diminished by 1.6% per year. The latter value was used for Buffington et al. (2007) calibration. Here, we adopt a compromise of 1% per year. When combining cameras or reporting surface-brightness measurements we use "normalized camera 2 units", referring to camera 2 at "mission start time" (taken as early 2003). This takes into account both responsivity differences between the cameras at mission start, and their subsequent degrading. At the beginning of the mission the multiplicative normalization factor to match camera 1 to camera 2 is 0.97, and 0.93 to match camera 3 to camera 2.

Bright stars are a significant feature in the SMEI data, but form a distracting source of noise when using these data to determine an appropriate zodiacal-light model. We have here employed a fitting-and-subtraction technique (Hick et al., 2005, 2007) to remove the brightest stars. As a starting point, we used the SIMBAD Astronomical Database, http://simbad.u-strasbg.fr/simbad/, to select stars having a visual magnitude brighter than 8th; we next use the manufacturer's quantum efficiency data for a CCD, and include light loss from 2 reflections off the aluminum mirrors, to calculate an effective scaling factor from visual magnitude to "smei magnitude". Thus, a list containing 5572 individual stars brighter than about 6th magnitude in SMEI was formed. This list was augmented by 37 Mira-type variable stars directly found in the SMEI data that sometimes appeared brighter than 6th magnitude. These then formed the selection of stars to be fitted and removed.

Next, a fainter-star residual sidereal background was subtracted; through this stage the sky maps had $0.1° \times 0.1°$ sky bins in equatorial coordinates (Hick et al., 2005; 2007). Appendix B details the fainter-star residual-background determination. These fully-subtracted sky maps were converted to Sun-centered ecliptic coordinates and binned up to an angular image bin size of $0.5° \times 0.5°$. Typically 14–15 of these individual-orbit maps were median-filtered to make a set of 2854 daily maps that were used for the present analysis. Interested readers may find these residual-sky maps at: http://smei.ucsd.edu/new_smei/data&images/zodiacal_data/. Also available at this location are the zodiacal-light maps shown here as Figs. 1 and 2, the sidereal background maps shown in Appendix B, and an illustrative sample of 365 daily zodiacal-light maps evaluated for noon, throughout the year 2003.

3. Zodiacal surface-brightness model

SMEI data over its first six years contributed to the present zodiacal surface-brightness model. This has an essentially *ad hoc* form and is parameterized in Sun-centered-ecliptic latitude and longitude, and quantities derived from these. This parameterization and subsequent parameter-value choices together yield a brightness result which matches well to the averaged observations. We do not attempt here to connect the choice of parameterization for this model to an actual distribution of interplanetary dust, or to take into account the optical scattering properties of such dust. Instead, the functional choices are simply governed by what fits the SMEI data best.

Our earlier analysis of the Gegenschein brightness (Buffington et al., 2009) compares the present model with the Celestial Background Scene Descriptor (CBSD) Zodiacal Emission Model "CBZodi" (Noah and Noah, 2001) and finds a good match when the Henyey-Greenstein (Hong, 1985) scattering function normally used by CBZodi is altered to include a backscatter function (Helfenstein et al., 1997). We note also that Kelsall et al. (1998) present a 3D physical zodiacal model. Our more modest aim here is a presentation to summarize the SMEI measurements for interested readers and researchers, extending our previous Gegenschein results to the rest of the sky.

The present model's coverage begins about 18° from the Sun and extends to the antisolar point. Zodiacal-light's wide-brightness-range over this domain led us to a hierarchical approach, including contributions from multiple formulae and from empirical residue tables. The present philosophy incorporates as much as possible into the formulae, and minimizes contributions from residual tables: this approach minimizes potential error contributions that may arise from interpolation between table entries.

The model (here) is mostly time independent but has some *ad hoc* time-dependent corrections and for camera 3 alone uses weekly residue maps in the solar hemisphere. The main calculation (Eq. (1)) explicitly includes a small slab-like annual term to account for the inclination of the plane of symmetry of the

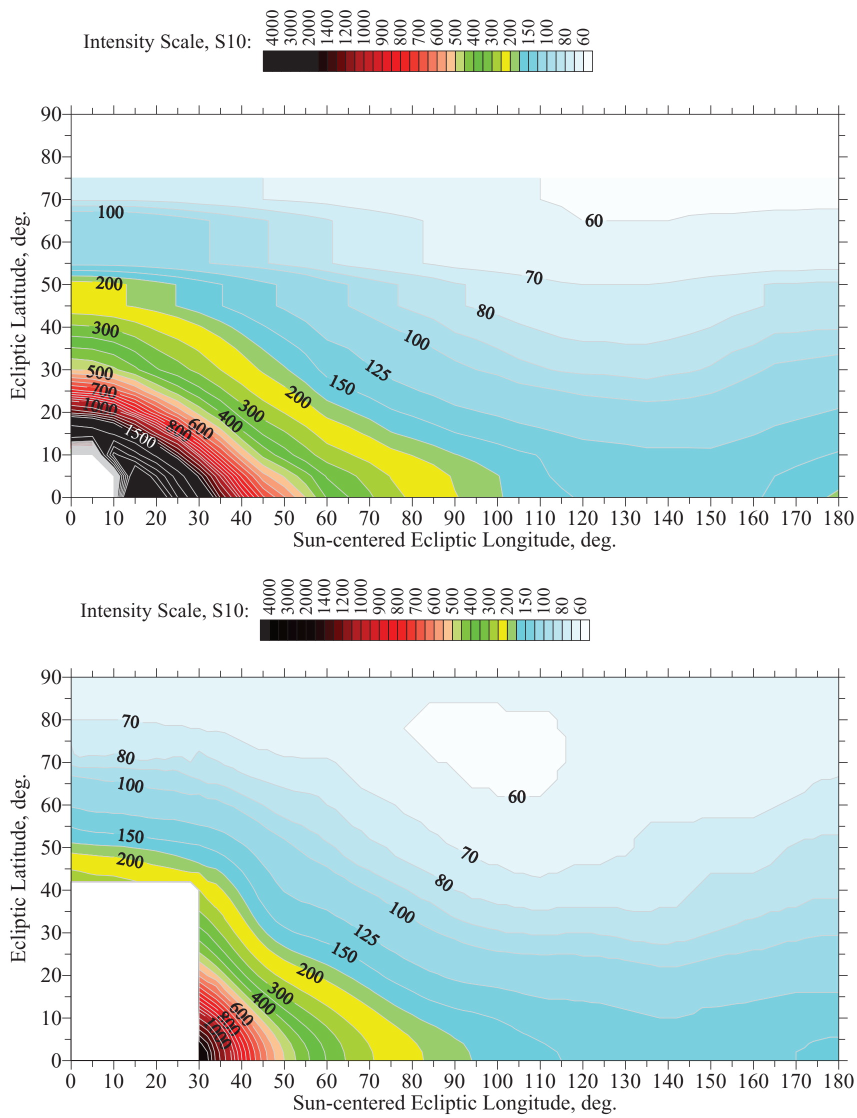

Fig. 1. Top: Zodiacal-light brightness (top) from Leinert et al. (1998), and (bottom) from Kwon et al. (2004). Angular bins here are 5° × 5° (top) and 2° × 2° (bottom).

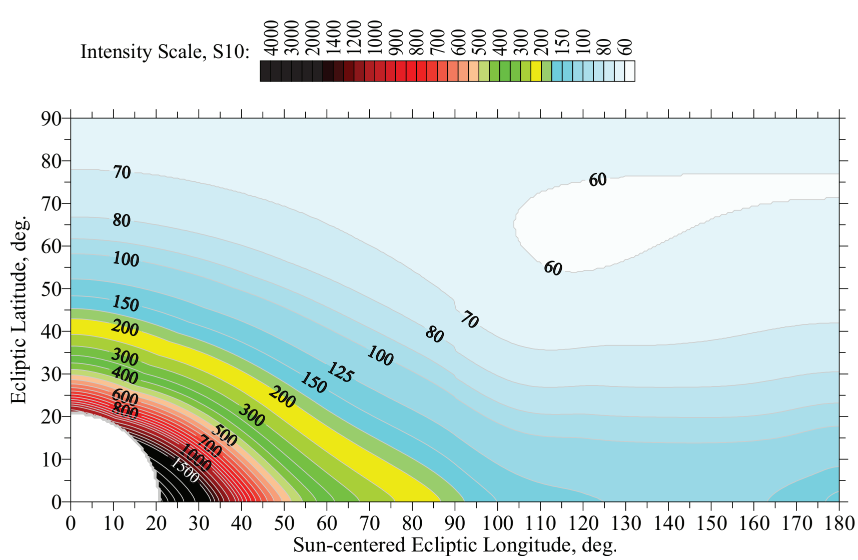

Fig. 2. This work. Modeled results are averaged over a period of a year, North and South are also averaged, and the ADUs of Section 3 have been divided by 0.46 to convert to S10 units. Although SMEI coverage sometimes extends to within 18° of the Sun, we here limit the presented result to > 20°. Angular bins here are 1° × 1°.

zodiacal dust relative to the ecliptic plane (Eq. (2)), and our previous Gegenschein results (Eqs. (3)–(5), see Buffington et al., 2009). Additionally, it includes an empirical "dumbbell"-shaped object aligned along the Sun's polar axis (Eqs. (C.1) and (C.2)), and finally for camera 3 only, an overall empirical residue map, some time-dependent *ad-hoc* corrections, and finally an interpolation between a set of empirical weekly maps to cover the last bits of residual difference between modeled results and the SMEI observations. The objective here was a removal of any sky brightness which repeats year after year in order to best-discern shorter-term and longer-term variations in the residue.

This models calculations are expressed in units of the previously-described SMEI ADUs. All angles are given in degrees. We use the ecliptic coordinate frame with longitude λ and latitude β, and define several auxiliary angles: $\boldsymbol{\lambda}_{Sun}$ is the ecliptic longitude of the Sun relative to the vernal equinox; $\tilde{\lambda} = (\lambda - \lambda_{Sun} - 180)$ is the antisolar ecliptic longitude; elongation ε is given by $c = \cos(\varepsilon) = \cos(\lambda - \lambda_{Sun})\cos(\beta)$, and antisolar elongation $\tilde{\varepsilon} = 180 - \varepsilon$; position angle γ, increasing counterclockwise from ecliptic North, is given by $\tan(\gamma) = \sin(\lambda - \lambda_{Sun})/\tan(\beta)$, and also $\cos\tilde{\varepsilon} = \cos\beta\cos\tilde{\lambda}$. The ecliptic longitude of the ascending node of the plane of symmetry of the zodiacal dust is here chosen to be $\Omega = 78.25°$ (Leinert et al., 1998; Cox 2000); Ω has a range of permissible values (Reach, 1988, 1991), but the present number is satisfactory for the SMEI data.

We further define $b = 1.5 \times (\sqrt{1 + (\beta/1.5)^2} - 1)$, and substitute this for$|\beta|$ where use of this latter would cause a cusp (discontinuity in the first derivative) in the ecliptic plane ($\beta = 0$). To indicate terms which are applied over only part of the sky, we use the Heaviside step function $u(x)$, where $u(x) = 0$ for $x \le 0$ and $u(x) = 1$ for $x > 0$. Thus $u(90{-}\varepsilon)$ is nonzero only in the sunward hemisphere and $u(\varepsilon{-}90)$ is nonzero only in the anti-solar hemisphere. Similarly, $u(\lambda_{Sun}{-}\Omega)$ is nonzero only when $0 < (\lambda_{Sun}{-}\Omega) \le 180$ (Earth above the plane of symmetry) and $u(\Omega{-}\lambda_{Sun})$ is nonzero only when $-180 \le (\Omega{-}\lambda_{Sun}) \le 0$ (Earth below the plane of symmetry). Finally, dependence on heliocentric (Sun–Earth) distance R is normalized to $R_0 = 1$ AU. In these terms, the modeled brightness Z for given values of λ, β and λ_{Sun} is thus:

$$\begin{aligned}(R_0/R)^{-2.3}Z &= 7 + 8(1-\cos b) + 6e^{-\beta^2/512}\\ &+ \left\{\begin{matrix} u(90-\varepsilon)\{65 + 120c - 185c^2 + 65c^3\}\sin^{-2.3}(\varepsilon) + \\ u(\varepsilon - 90)\{65 + 120c + 154c^2 + 88c^3\}\end{matrix}\right\}\\ &\times 10^{-\{\frac{\sin b}{0.009(\varepsilon+40)}\}} + u(90-\varepsilon)\{30(\sin^{-2.3}(\varepsilon) - 1)\cos b\}\\ &+ \left\{8800e^{+\{1-\sqrt{1+((|\gamma|-90)/3)^2}\}/10} - 1200\right\} \times e^{-\varepsilon/10}\\ &+ S(\lambda_{Sun}, \Omega, \varepsilon) + D(\lambda - \lambda_{Sun}, \beta) + E + F(\lambda_{Sun}) + G(\beta, \tilde{\lambda}). \quad (1)\end{aligned}$$

The $S(\lambda_{Sun}, \Omega, \varepsilon)$ term provides a slab whose maximum brightness is 6 ADUs. This moves back and forth between North and South over the course of a year, is brighter in the South than the North, and is placed above or below the ecliptic and also "feathered" across it, over $\pm 5°$. Here,

$$\begin{aligned}S(\lambda_{Sun}, \Omega, \varepsilon) = 6|\sin(\lambda_{Sun} - \Omega)|&\\ \times [u(90-\varepsilon)\sin^{-2.3}(\varepsilon) + u(\varepsilon - 90)\sin\varepsilon]&\\ \times [1 - u(\Omega - \lambda_{Sun})/4 + 2u(90-\varepsilon)c]&\\ \times \max(0, \min([\{u(\Omega - \lambda_{Sun})&\\ - u(\lambda_{Sun} - \Omega)\}\beta + 5)]/10, 1)).& \quad (2)\end{aligned}$$

where, "max" denotes the greater of the two entries within the appropriate parentheses, and similarly "min" the lesser of the two entries. The empirical dumbbell-shaped $D(\lambda - \lambda_{Sun}, \beta)$ incorporates as much as possible of what's left into an analytic formula, and the final-residual terms E and $F(\boldsymbol{\lambda}_{Sun})$ are maps for the towards-the-Sun hemisphere whose proper look-up-table entries are determined by $\lambda{-}\lambda_{Sun}$ and β. These three items are described in Appendix B. Finally, the $G(\beta, \tilde{\lambda})$ term explicitly includes the "Gegenschein enhancement" (Buffington et al., 2009) with

$$\begin{aligned}G(\beta, \tilde{\lambda}) = (1 - 0.02(\beta\tilde{\lambda}^2)/\tilde{\varepsilon}^3) \times (\beta^2 G_\beta + \tilde{\lambda}^2 G_{\tilde{\lambda}})/\tilde{\varepsilon}^2&\\ \times \left\{1 - u(\tilde{\varepsilon} - 60) \times \left(1 - e^{-\{(\tilde{\varepsilon}-60)^2/300\}}\right)\right\},& \quad (3)\end{aligned}$$

where

$$G_\beta = 7.5e^{-\tilde{\varepsilon}/4} + 39.5e^{-\tilde{\varepsilon}/25} \quad , \quad (4)$$

$$G_{\tilde{\lambda}} = 7.5e^{-\tilde{\varepsilon}/4} + 39.5e^{-\tilde{\varepsilon}/35} \quad . \quad (5)$$

In the antisolar hemisphere these equations are essentially unchanged from those in Buffington et al. (2009). Here, the addition of the final term in Eq. (3) smoothly decreases the Gegenschein enhancement contribution for $\tilde{\varepsilon} \ge 60$, so as to render it negligible in the Sunward hemisphere.

4. Comparison of the model with previous measurements

The parameterized model described above can be compared with earlier zodiacal-light results. Leinert et al. (1998) and Kwon et al. (2004) both provide convenient tabular summaries which we present here as Fig. 1. The present SMEI-based model is shown in Fig. 2. Here East and West halves are assumed to be the same, the dumbbell-shaped contribution from Eq. (C.2) and Fig. (C1) is averaged between North and South. Our results from Eq. (1) are (10 ± 10)% less than those from Leinert et al. and from Kwon et al.: a better match to these would be provided by adding an extra 6 ADUs (13 S10s) to Eq. (1). This discrepancy may result from our having omitted the $S(\lambda_{Sun}, \Omega, \varepsilon)$ slab term for Fig. 2. Of the variety of models discussed in Giese et al., (1986), the present data most resemble the "modified fan model" of Lumme and Bowell (1985).

5. Analysis of three sidereal objects

A confirmed long-term change in SMEI data for various sky locations might indicate interesting secular changes in the zodiacal-dust-cloud distribution. However, this could also simply result from the actual SMEI responsivity change with time being different from the 1% per year here assumed. To restrict this possibility, we have chosen three stable sky regions which, upon their zodiacal-light contribution being removed, serve as photometric references. These are: (1) the Andromeda Galaxy, (2) the Small Magellanic Cloud (SMC), and (3) the Large Magellanic Cloud (LMC). Contour plots of these, derived from Fig. B2, are illustrated in Fig. 3. We have least-squares fitted these profiles to fully-subtracted residue maps for SMEI daily-average data, as was done for the Gegenschein in Buffington et al. (2009). Fig. 4 and Table 1 illustrate the result. As expected, although an annual variation of order several ADUs persists for each of these objects, no significant further long-term differential photometric accuracy trend is seen down to about 0.25% of the mean brightness for each object over the SMEI data span.

6. Potential variation of zodiacal-light brightness with time

Our previous article (Buffington et al., 2009) reported a ~10% variability in the minimum- χ^2 fitted brightness of the Gegenschein, most of it annually repeating. Figs. 5–7 present plots of χ^2/f, offset brightness N, and peak Gegenschein brightness. Here, as in Eq. (8) of the previous article, the sum forming χ^2 has f ~30,000 bins, so χ^2 is normalized by dividing by f. These update the corresponding figures in Buffington et al. (2009) to include all SMEI data versus DOY. Here also cameras 1 and 2 are combined, and not just camera 1 as in that previous article. Including both

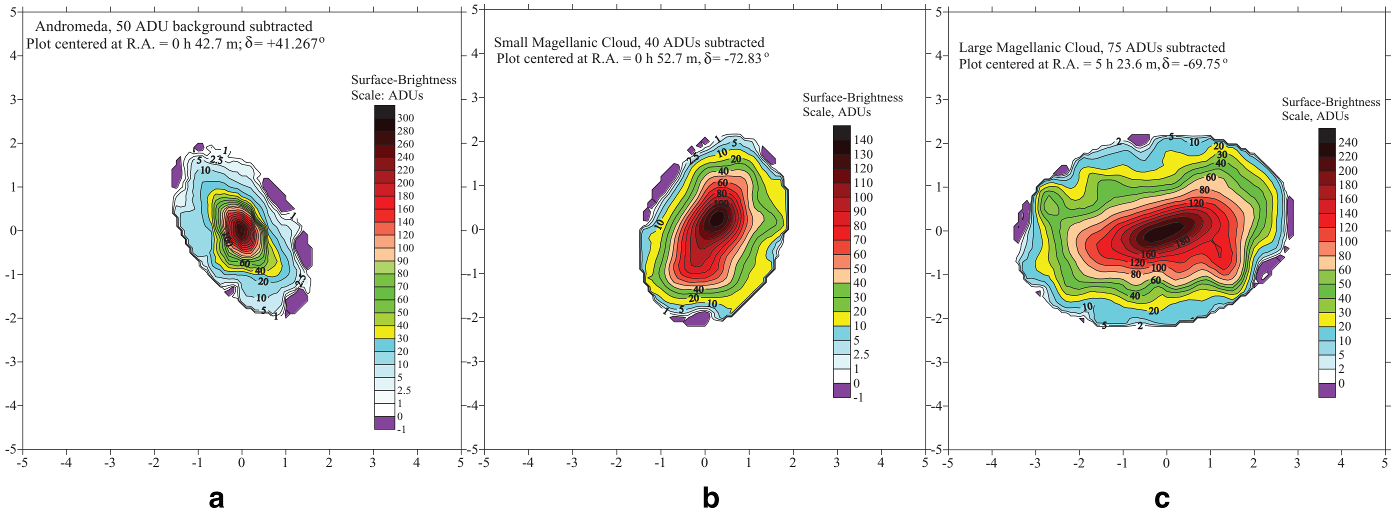

Fig. 3. SMEI sky brightness near three sidereal objects versus sky angle (degrees). (a) Andromeda Galaxy; (b) SMC; (c) LMC. Each shows the chosen elliptical photometric window and contours of brightness within. As in Fig. 2, ADU brightness divided by 0.46 converts to S10 units. Scales here are degrees of angular sky displacement from the center of each, respectively along R.A. (X-axis) and declination δ (Y-axis). In (b) and (c), positive displacement in δ is toward the south as in the southern map of Fig. B2 here.

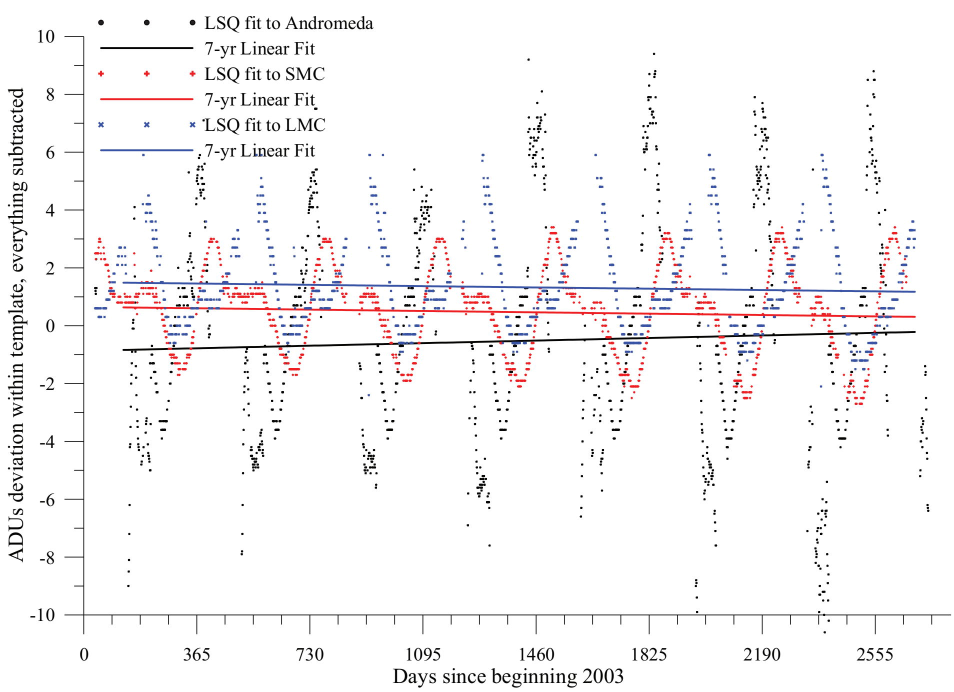

Fig. 4. A plot of average fitted residue above background for the indicated three sky objects, versus elapsed days since the beginning of year 2003. To minimize systematic error that might enter through inclusion of an incomplete year, all the linear fits start at DOY 128 of 2003 and extend through to the same day in 2010.

Table 1
Sidereal objects. Location, size, and fitted brightness change covering 7.0 years beginning on DOY 128 in 2003.

Sidereal objects	R.A. (hh mm)	Decl. δ (°)	Size (°)	Obs. slope (ADUs/day)	Brightness peak. val. [a]	Fractional change/day
Andromeda	00 43	+41.3	2.5×4.5	+.00024	300 ADUs	$+8 \times 10^{-7}$
SMC	00 53	−72.8	3.5×4.5	−.00013	145 ADUs	-8×10^{-7}
LMC	05 24	−79.8	6.5×4.5	−.00012	250 ADUs	-5×10^{-7}

[a] To convert ADUs to S10 units, divide the above values by 0.46.

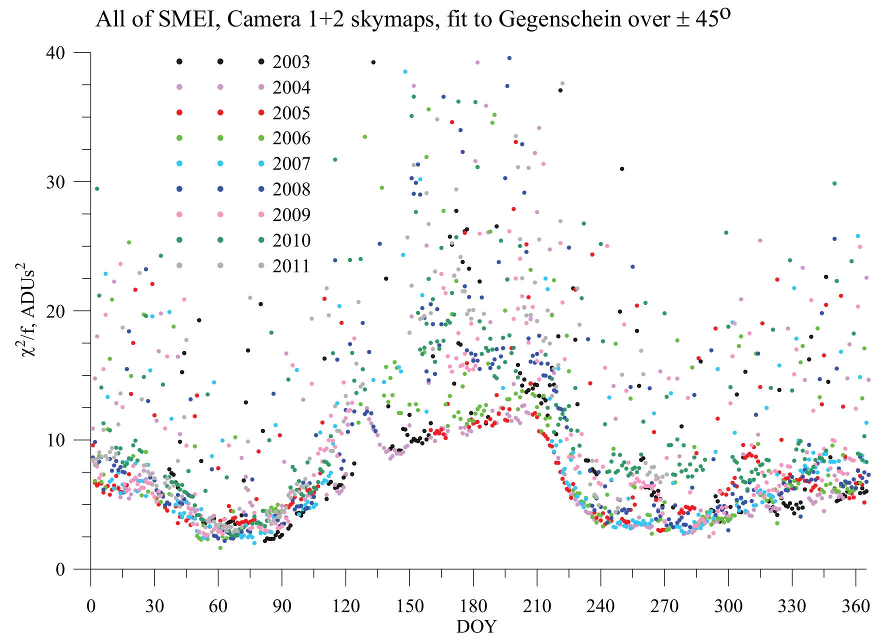

Fig. 5. Gegenschein. A plot of χ^2/f versus DOY. As before, broad peaks near mid- and end-year are expected, since this is the time when the antisolar point passes over the Galactic plane. This both increases noise and can introduce systematic error due to uncertainty in the cameras' responsivity as this bright portion of sky passes by.

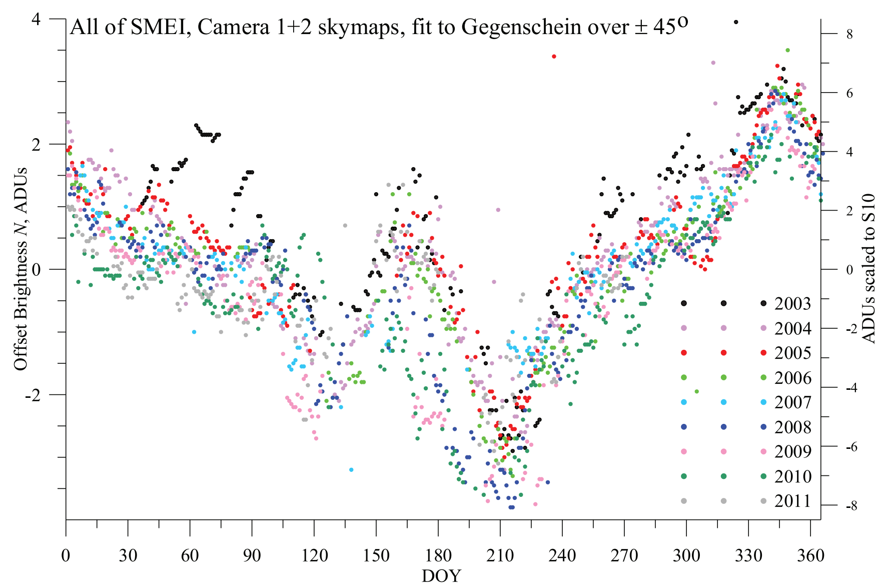

Fig. 6. Gegenschein. Offset N versus DOY. Like χ^2/f, the offset N varies systematically over the course of a year. The ±3 ADU variation here could be due to an actual variation with DOY of the larger-scale content of the zodiacal light, or to a residual in the sidereal-sky subtractions.

cameras significantly increases the number of daily maps meeting our analysis criteria, although some of the added maps have a larger-than-usual χ^2/f, as can be seen in Fig. 5. Due to its higher noise contribution, no attempt is made here to include data from camera 3.

The SMEI dataset spans a total of 3157 days. Figs. 8 and 9 unfold the data of Figs. 6 and 7 respectively, to display the results of fitted Gegenschein offset and peak brightness over the full SMEI time period. The observed slope for Gegenschein peak brightness in Fig. 9 amounts to a total change over this time of only 0.135 ADUs, which when compared with the measured peak brightness of 43 ADUs, yields an apparent change in this fitted quantity of only 0.3% over the SMEI lifetime. The associated offset brightness change, from Fig. 8, is somewhat larger, about 1 ADU.

Figs. 10–14 show the brightness changes at eight additional ecliptic locations in the sky, using combined data from cameras 1 and 2. Table 2 summarizes the long-term changes observed in all these data. These are typically several $\times 10^{-4}$ ADUs per day, some increasing, some decreasing.

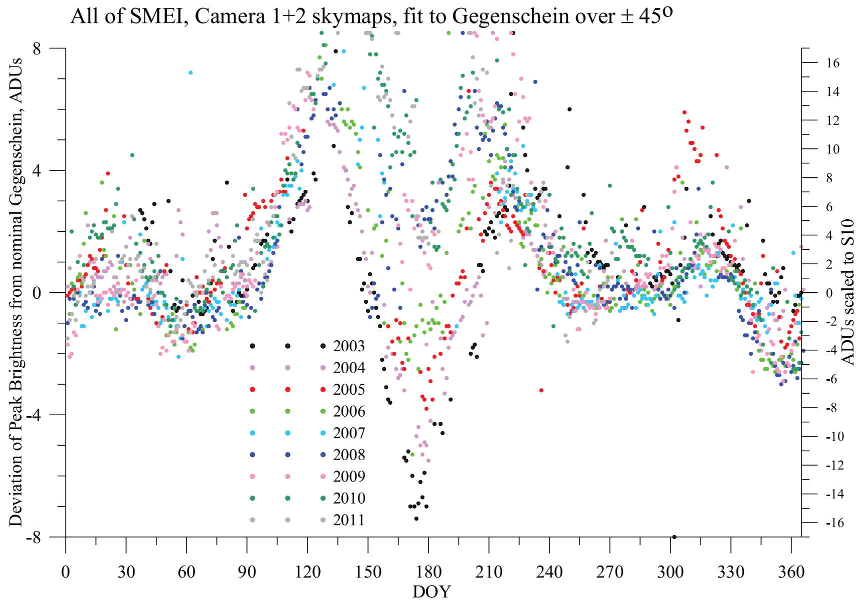

Fig. 7. Gegenschein. Deviation of peak fitted brightness ($MG_{tot}(0,0)$) from a nominal value of 43 ADUs, versus DOY. As previously reported (Buffington et al., 2009), considerable structure through the course of a year is visible, but here the inclusion of camera 2 data is seen to have tightened up the year-to-year variation considerably. The roughly 8 ADU decrease with time near the Galactic Center (DOY 170) is likely a systematic effect, given this bright sky, which changes the cameras' response from the nominal 1%/year used in the present analysis.

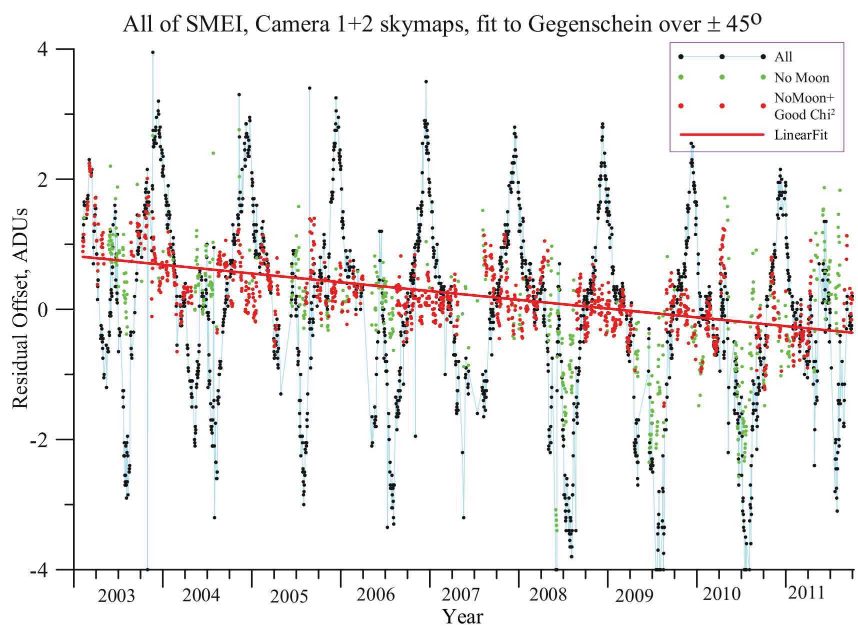

Fig. 8. Fig. 6 unfolded to display the full time spanned by the SMEI data. Here for "No Moon" the daily values were omitted within ± 5 days of full Moon, and for "Good Chi²" also that $\chi^2/f < 8.5$. The long-term slope of the latter (red line) is -3.7×10^{-4} ADUs per day. (For interpretation of the references to color in this figure legend, the reader is referred to the web version of this article).

6. Discussion

Assuming an unchanging distribution of the zodiacal light enables averaging together all the SMEI results of Table 2: this provides a zodiacal-light upper limit to change over the 8.5 years of data, of only 0.22%, -7×10^{-7} per day. Combining this in quadrature with the sidereal certification in Section 5 yields an overall 1−σ upper limit of about 0.3% to zodiacal-light brightness change over this time period. A preliminary report of this work was presented at the 2011 Fall AGU meeting (http://abstractsearch.agu.org/meetings/2011/FM/SH13B-1970.html).

Dumont and Levasseur-Regourd (1978) place a limit of 10% on secular change of the zodiacal light over one solar cycle. Leinert and Pitz (1989) also report an upper limit (±1.5% over 11 years, i.e. 3.7×10^{-6} per day) to potential change, using Helios measurements that were viewing a $1° \times 5.6°$ patch of sky at elongations of $\varepsilon = 16°$ and 63° from the Sun. These authors conclude that "the zodiacal light is remarkably stable" and at this

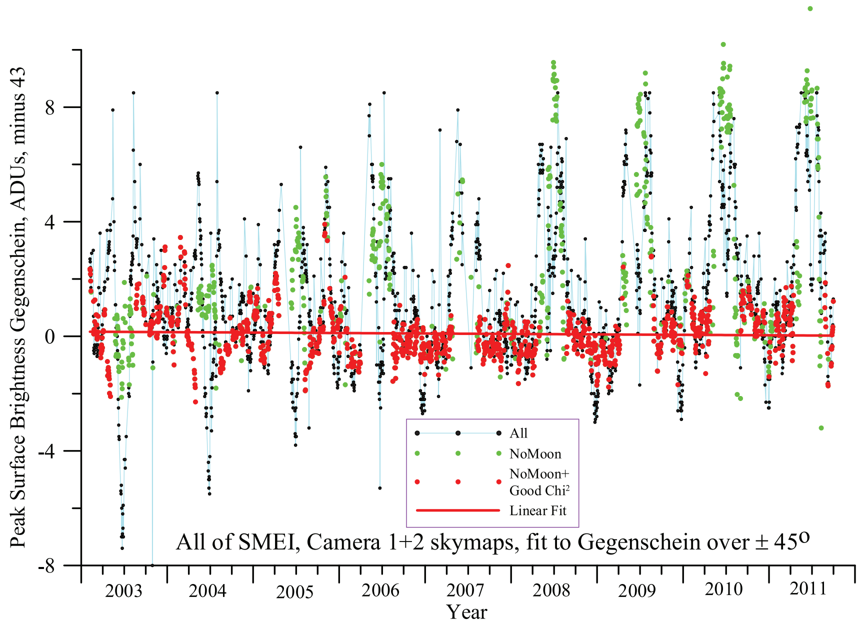

Fig. 9. Similar to Fig. 8, but for the Gegenschein fitted-peak brightness. Here the long-term slope is -4.3×10^{-5} ADUs per day.

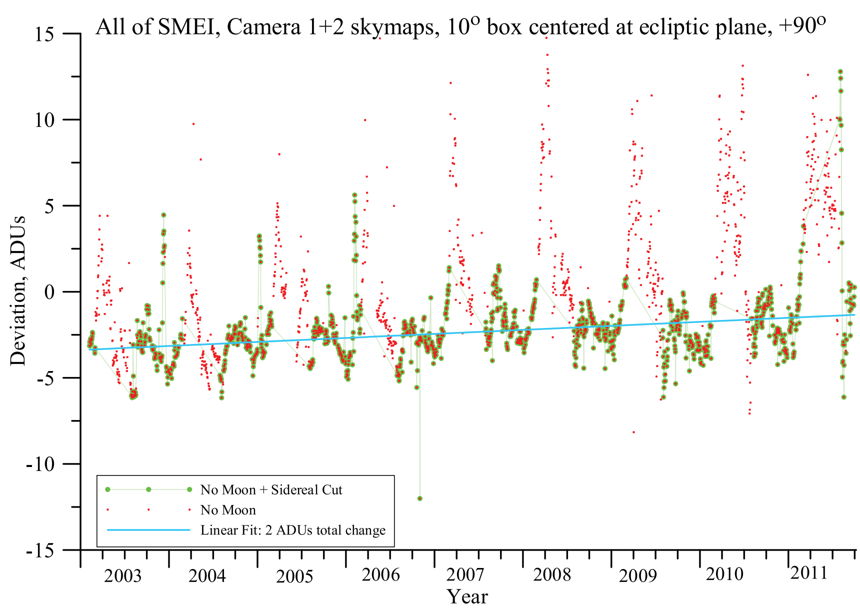

Fig. 10. Residual brightness for a 10° square on the ecliptic plane at longitude 90°.

Table 2
Ecliptic-coordinate objects. Location, size, and observed brightness change.

Name	Ecliptic longitude	Ecliptic latitude	Size (deg)	Obs. slope, ADUs/day	Zodiacal Brightness[a]	Fractional change/day[b]
Gegenschein						
Peak	180°	N/A	±45°	−.00004	43 ADUs	-9×10^{-7}
Offset	180°	N/A	±45°	−.00037	100 ADUs	-3.7×10^{-6}
N. Pole	N/A	+90°	10° dia.	−.00050	62 ADUs	-8.1×10^{-6}
S. Pole	N/A	−90°	"	−.00025	"	-4.0×10^{-6}
Ecliptic plane	90°	0°	±5°	+.00064	190 ADUs	$+3.4 \times 10^{-6}$
	270°	0°	"	+.00044	"	$+2.3 \times 10^{-6}$
	90°	+30°	"	$+3 \times 10^{-7}$	90 ADUs	$+3 \times 10^{-9}$
	270°	+30°	"	−.00030	"	-3.3×10^{-6}
	90°	−30°	"	+.00065	"	$+7.2 \times 10^{-6}$
	270°	−30°	"	+.00004	"	$+4 \times 10^{-7}$

[a] Annual Average: to convert ADUs to S10 units, divide the above values by 0.46.
[b] Note that this daily change does not include in the fraction, any extra brightness from the sidereal background (presumably unchanging from year to year), but would alter the result in the event that the presently assumed 1%/year reduction in detector responsivity is not correct.

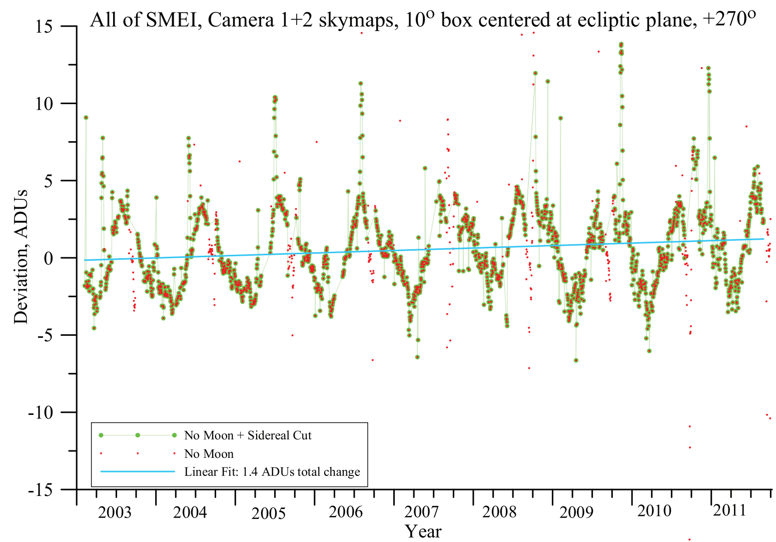

Fig. 11. Residual brightness for a 10° square on the ecliptic plane at longitude 270°.

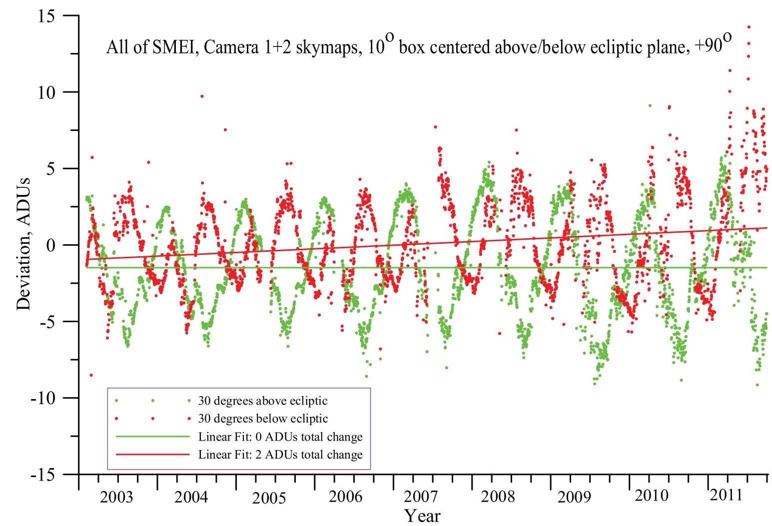

Fig. 12. Residual brightness for a 10° square with latitude 30° above/below the ecliptic plane at longitude 90°.

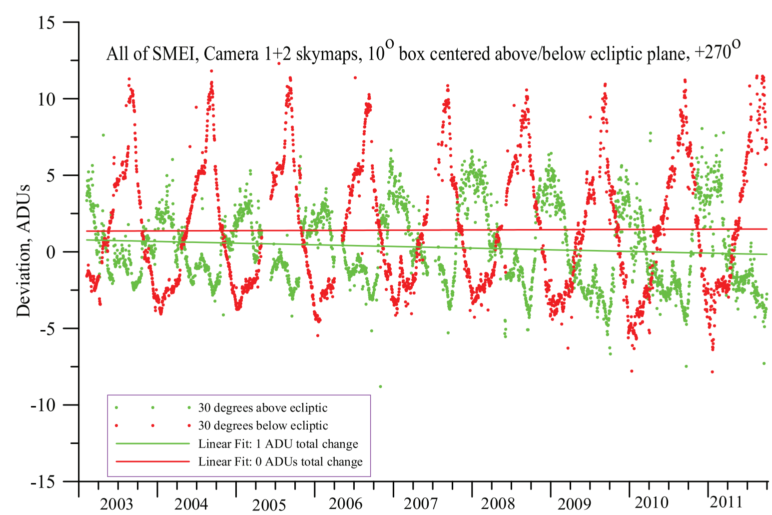

Fig. 13. Residual brightness for a 10° square with latitude 30° above/below the ecliptic plane at longitude 270°.

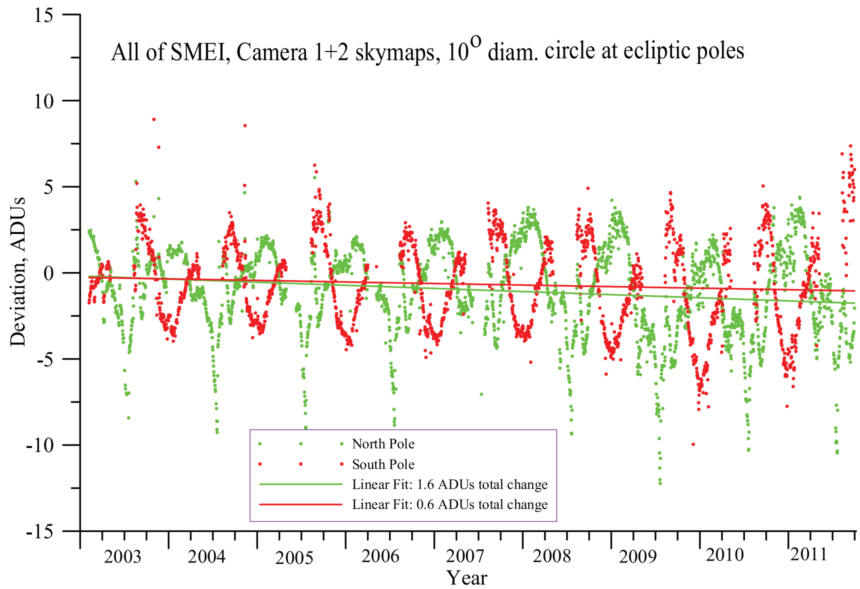

Fig. 14. Residual brightness for a 10º diameter circle at the ecliptic poles.

accuracy "start to constrain collisional models for interplanetary dust." The present result extends this constraint to many other sky locations, and together tightens this apparent stability by a factor of three to five. To maintain zodiacal-dust density stability of better than 1% over a significant fraction of a solar cycle most likely indicates that the variable solar-wind density is unlikely to play a dominant role in the replenishment of zodiacal dust. Moreover, it casts further doubt on hypotheses where dust replenishment depends on cometary passages and perhaps even asteroid collisions (see discussion in Leinert and Grün, 1990, pp. 254–264).

The present work extends a comparable upper limit to other sky locations including the antisolar point; the ecliptic poles; and various locations along, and above and below, the ecliptic. In each case no significant secular change in zodiacal light brightness is observed. As noted in Section 3, the "model" presented here is unlike 3-D physical zodiacal models such as that of Kelsall et al. (1998), or CBZodi (Noah and Noah, 2001). Instead, it merely provides a convenient representation for summarizing the SMEI zodiacal-light measurement results. A key question: which of the various terms in Eq. (1) are really "up in the sky" and which are merely SMEI instrumental artifacts? We feel that the main equation and terms S and G of this equation are almost all "up in the sky", whereas D and E are probably mixed with instrumental artifacts, and F is almost all due to stray-light residues in camera 3 and thus specific to SMEI and not "up in the sky".

Acknowledgments

SMEI was designed and constructed by a team of scientists and engineers from the US Air Force Research Laboratory, the University of California at San Diego, Boston College, Boston University, and the University of Birmingham in the UK. The present work was supported in part by Grants NSF AGS1053766 and NASA NNX14AC11G.

Appendix A. The SMEI optics

The SMEI optics were briefly described in Eyles et al. (2003); here, for completeness, we present a more-detailed description and specify the mirror-surface equations. Figs. A1 and A2 are an

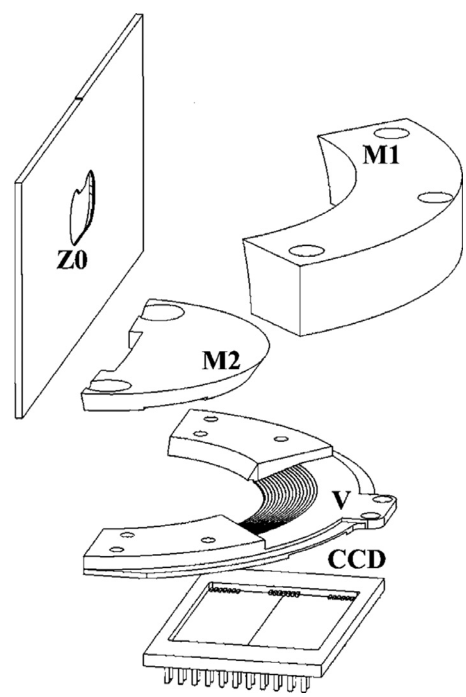

Fig. A1. Exploded diagram of the SMEI optics (adapted from Eyles et al., 2003).

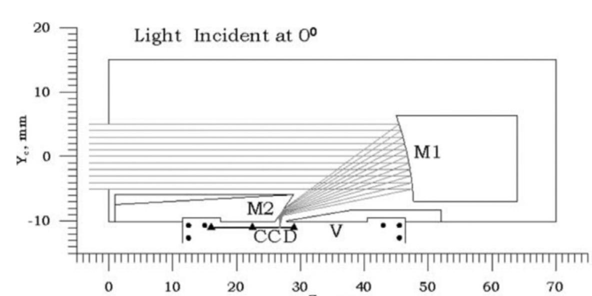

Fig. A2. A cross-section through the optical system showing normally-incident light entering through the photometric aperture (Z0) and focused upon the CCD (adapted from Eyles et al., 2003).

exploded diagram of the optics and a cross-section in a central plane containing its axis of rotation. To achieve the large field of view, the SMEI optical system has a very fast design. Light enters through the photometric aperture Z0; primary mirror M1 focuses this off the secondary mirror M2 to the 1242×576 pixel CCD.

In the coordinate frame of Fig. A2, the surface of mirror M1 is defined by

$$|Z_c| = 47.8 - \frac{(Y_c + 9.5)^2}{90.4} - 10^{-7} \times (Y_c + 9.5)^4. \quad \text{(A.1)}$$

Units are millimeters. The maximum and minimum values of Z_c upon mirror M2 are respectively 28.934 and 26.042. Both M1 and M2 are rotated about the Y-axis of this diagram to generate the full reflecting surfaces shown in Fig. A1. The surface of mirror M2 is on a cone whose vertex half-angle is 35°. Reflecting surfaces are diamond-turned without post-polishing, to minimize light scattering beyond a few degrees.

The short dimension of the M1 mirror is an $f/2.2$ off-axis parabola while the long dimension is figured as an $f/1.2$ cylindrical mirror. The parabola has a focus in front of the CCD while the focus of the cylindrical mirror converges behind the CCD; this configuration adequately controls the photometric consequences of hot spots in the point spread functions (PSFs) that typically result from very fast optics. An unresolved (point source) image is shown in Fig. A3 (top) and has an effective area of ~0.5 deg². The field of view is also distorted, straight cross-scan lines of constant angle are curved into arcs. Thus, not only do the detailed shapes of the point-spread functions change versus position in the focal plane (Fig. A3, bottom), but also this optics transforms a line of roughly constant cross-scan angle into an arc on the CCD.

Appendix B. Determination of sidereal background for SMEI

SMEI calibration data were taken roughly bi-monthly for each camera with onboard binning switched off so that all pixels for a given camera were available for analyses. Due to telemetry limitations, data in this mode were returned from only one camera at a time (Eyles et al., 2003). A typical calibration includes one day's 14–15 orbits for each camera. For a given camera and each calibration period, a sky map is formed in Right Ascension (RA) and Declination (δ), which for each pixel in the map is the median of the individual-orbit values for that pixel's location after the parameterized zodiacal light (Section 3) and 5609 bright stars are subtracted. Use of the median minimizes possible contamination from SAA and auroral-oval particles that survived formation of the individual-orbit sky maps; the median also reduces contamination from auroral light (Mizuno et al., 2005) as it moves over the maps through the course of a day. Towards the end of the mission, calibrations were taken less frequently. Over the roughly 8.5-year course of SMEI data presented in this work, 36 such daily maps were generated for each camera. The final sidereal residue, which is subtracted within the main SMEI data-analysis pipeline, is an average of the camera 1 and 2 maps. Camera 3 data are not included in this average because this camera views much brighter zodiacal light and also suffers an elevated noise level since it operated hotter than the others. Figs. B1 and B2 show the sidereal residue, respectively, with the bright stars included and excluded. Fig. B2 is the one used in our SMEI data-analysis pipeline (Hick et al., 2005).

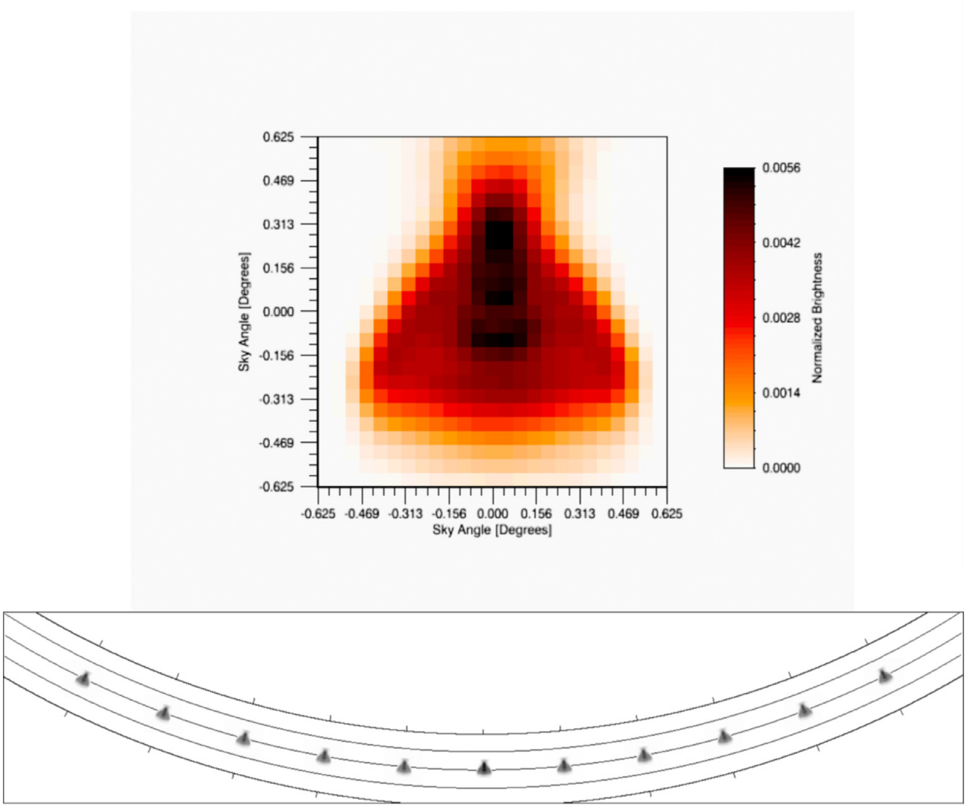

Fig. A3. (Top) A 25×25 pixel engineering-mode full-resolution image spanning $1.25° \times 1.25°$. (Bottom) Upon the CCD, the PSF is position dependent; it is rotated for local position along the FOV's long dimension and is slightly larger at the center. This figure shows a model of a star placed at different angles along the center of the FOV's narrow dimension. The curved lines mark position along the FOV long dimension with tic marks at roughly 5° intervals. Although the optics views a swath of sky about 6° wide in the FOV's narrow dimension, only a 3° wide band of sky within this is utilized for the full SMEI photometry.

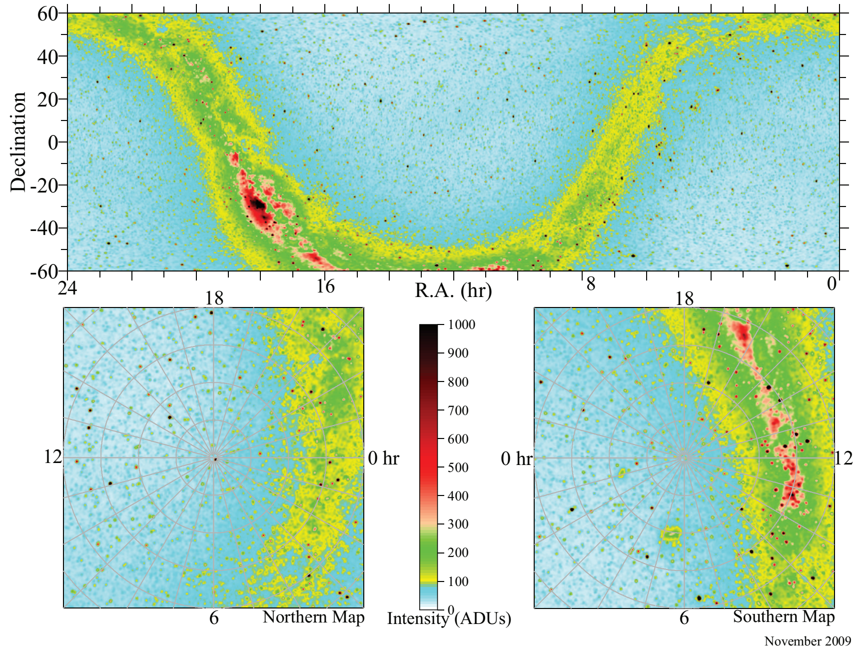

Fig. B1. Sidereal Sky as viewed by SMEI.

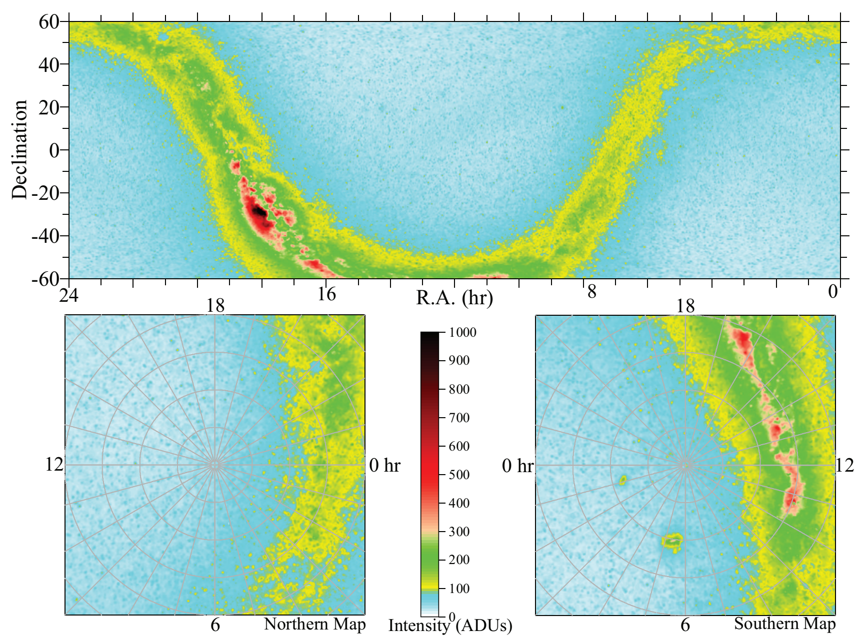

Fig. B2. The same as Fig. B1, but with the bright stars removed.

These maps include the bright stars of the familiar constellations. Polar maps follow the convention of "Norton's 2000.0" (I. Ridpath ed., Wiley, New York 1989); angles are in degrees. North and South Poles are centered in their respective Maps, where circles mark 10° intervals. The intensity scale is SMEI ADUs (see Section 2). Thus the transition in color from red to black corresponds here roughly to 3rd magnitude. These relative brightnesses differ from those in familiar visual-magnitude star atlases, because the bandpass of the SMEI cameras lies more to red wavelengths.

Fig. B2's maps are the ones used for sidereal-background subtraction in the normal SMEI data-analysis pipeline, where individually-fitted stars have been subtracted.

Appendix C. Terms *D*, *E*, and *F* in Eq. (1)

Eq. (1) was optimized while excluding $D(\lambda - \lambda_{Sun}, \beta)$, E, and $F(\boldsymbol{\lambda}_{Sun})$, to best fit the observed zodiacal-light distribution and thus, when subtracted, minimize the residue subsequently to be covered by these remaining three terms. The ε- and b-dependent portions of Eq. (1) match the SMEI measurements pretty well along the ecliptic, at the poles, and throughout the antisolar hemisphere. However, towards the Sun but also away from the ecliptic and poles, they do not fit as well. $D(\lambda - \lambda_{Sun}, \beta)$ introduces an analytic *ad hoc* "dumbbell" formula to improve this which, when subtracted, further reduces the zodiacal light remaining in these troublesome locations toward the Sun. What's left, hopefully minimized as much as possible, is finally covered in look-up-table

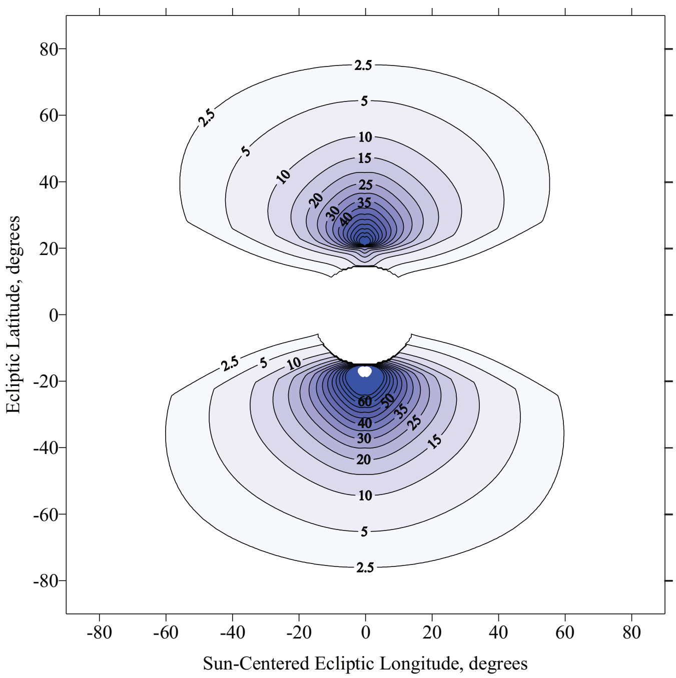

Fig. C1. A contour plot of $D(\lambda - \lambda_{Sun}, \beta)$. Intensity units are SMEI ADUs.

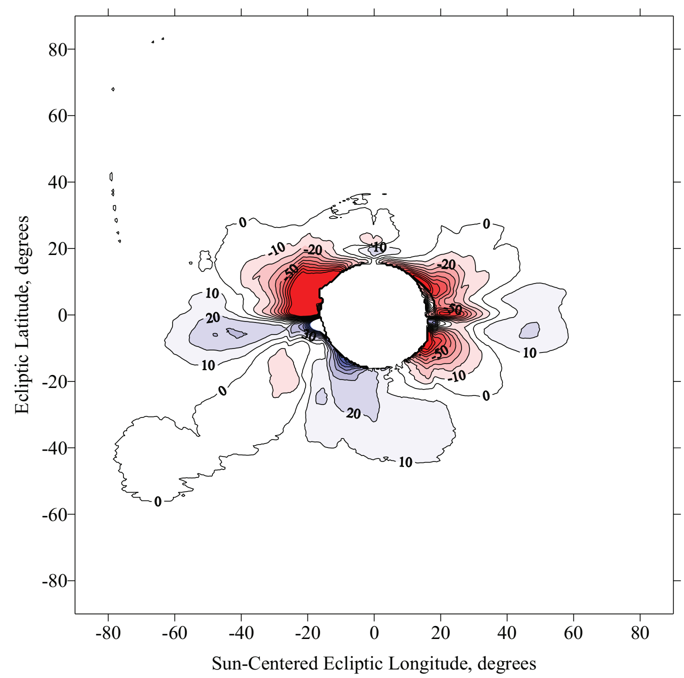

Fig. C2. The average annual residue, term E in Eq. (1). Intensity units are SMEI ADUs.

formed by the annual average E, and by the interpolated weekly residue $F(\boldsymbol{\lambda}_{Sun})$.

Parameterization of $D(\lambda - \lambda_{Sun}, \beta)$ proceeds similar to that of the other quantities in Eq. (1). Let $d = (|\lambda - \lambda_{Sun}|/6.5) - |\beta| + 15 + 5 \times u(\beta)$, where $u(x)$ is as previously defined, just before Eq. (1) above. Further, define new longitude λ', latitude β', elongation ε' and position angle γ'; relative to a direction 21° towards ecliptic north of the Sun ($\lambda = \lambda_{Sun}, \beta_0 = +21^\circ$) when $\beta > 0$, and relative to a direction 15° towards ecliptic south of the Sun ($\lambda = \lambda_{Sun}, \beta_0 = -15^\circ$) when $\beta < 0$. Next, let

$$\begin{aligned} h &= \gamma' \times u(-\beta) + (180 - \gamma') \times u(\beta), \\ A &= \{1 + 0.5 \times u(-\beta)\} \times u(90 - \varepsilon) \\ &\quad \times \{u(75 - \varepsilon) + u(\varepsilon - 75) \times e^{-(\varepsilon-75)^2/120}\}, \\ f(\varepsilon', h) &= 60 \times e^{-\varepsilon'/16} \times \{0.15 + 0.85e^{-6\cos^4(0.6h)}\}, \\ g(\lambda', \beta') &= 25 \times e^{-[\arccos(\cos 2\lambda' \times \cos(0.7\beta'))/10]}, \end{aligned} \tag{C.1}$$

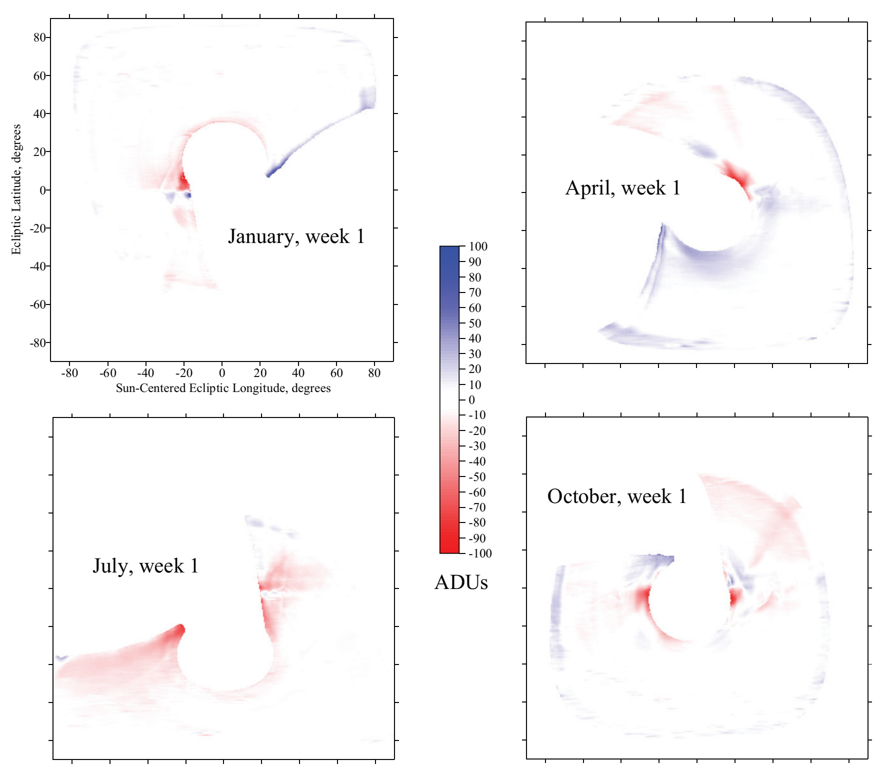

Fig. C3. Four examples of weekly residue maps, term $F(\boldsymbol{\lambda}_{Sun})$.

and finally

$$D(\lambda - \lambda_{Sun}, \beta) = A \times \{[f \times e^{-d/10} + g \times e^{-d/8}] \times u(d) + [f + g] \times u(-d)\}. \quad \text{(C.2)}$$

Fig. C1 is a contour map of the "dumbbell" $D(\lambda - \lambda_{Sun}, \beta)$, from Eq. (C.2).

Fig. C2 shows the six-year-average annual residue map, term E in Eq. (1). This map includes the difficult-to-parameterize region both close to the ecliptic and close to the Sun. The apparent asymmetry between East and West is most likely due to the uneven sky coverage of the SMEI camera 3 over the course of a year. This is caused by data regions too near the Sun being systematically excluded by the SMEI shutter.

Fig. C3 shows a sample of the weekly residue maps. Note that this series of 52 maps through the year is applied only to camera 3 data, and for a given date is interpolated between the nearest two maps. Most features in these maps are probably not real zodiacal-light structures, but instead stray-light artifacts, particularly near the closed-shutter exclusion zones, towards the Sun, and near the inner and outer edges of the field of view.

References

Buffington, A., Band, D.L., Jackson, B.V., et al., 2006. A search for early optical emission at gamma-ray burst locations by the Solar Mass Ejection Imager (SMEI). Astrophys. J. 637, 880–888.

Buffington, A., Morrill, J.S., Hick, P.P., et al., 2007. Analyses of the comparative responses of SMEI and LASCO. Proc. SPIE 66890B, 1–6. doi:10.1117/12.734658.

Buffington, A., Bisi, M.M., Clover, J.M., et al., 2008. Analysis of plasma-tail motions for comets C/2001 Q4 (NEAT) and C/2002 T7 (LINEAR) using observations from SMEI. Astrophys. J. 677, 798–807.

Buffington, A., Bisi, M.M., Clover, J.M., et al., 2009. Measurements of the gegenschein brightness from the Solar Mass Ejection Imager (SMEI). Icarus 203, 124–133. doi:10.1016/j.icarus.2009.04.007.

Cox, A.N., 2000. Allen's Astrophysical Quantities, fourth ed. Springer-Verlag, New York, p. 330.

Dumont, R., Levasseur-Regourd, A.C., 1978. Zodiacal light photopolarimetry IV. Annual variations of brightness and the symmetry plane of the zodiacal cloud, absence of solar cycle variation. Astron. Astrophys. 64, 9–16.

Eyles, C.J., Simnett, G.M., Cooke, M.P., et al., 2003. The Solar Mass Ejection Imager (SMEI). Sol. Phys 217, 319–347.

Giese, R.H., Kneissel, B., Rittich, U., 1986. Three-dimensional models of the zodiacal dust cloud: A comparative study. Icarus 68, 395–411.

Helfenstein, P., Ververka, J., Hillier, J., 1997. The Lunar opposition effect: A test of alternative models. Icarus 128, 2–14.

Hick, P.P., Buffington, A., Jackson, B.V., 2005. The SMEI real-time data pipeline: From raw CCD frames to photometrically accurate full-sky maps. Proc. SPIE 59011B, 1–7. doi:10.1117/12.617996.

Hick, P.P., Buffington, A., Jackson, B.V., 2007. A procedure for fitting point sources in SMEI white-light full-sky maps. Proc. SPIE 66890C, 1–8. doi:10.1117/12.734808.

Hong, S.S., 1985. Henyey-Greenstein representation of the mean volume scattering phase function for zodiacal dust. Astron. Astrophys. 146, 67–75.

Howard, T.A., Bisi, M.M., Buffington, A., et al., 2013. The solar mass ejection imager and its heliospheric imaging legacy. Space Sci. Rev. 180, 1–38. doi:10.1007/s 11214-013-9992-7.

Jackson, B.V., Bisi, M.M., Hick, P.P., et al., 2008. Solar Mass Ejection Imager (SMEI) 3D reconstruction of the 27–28 May 2003 CME sequence. J. Geophys. Res. 113, A00A15, 1–14. doi:10.1029/2008JA013224.

Jackson, B.V., Buffington, A., Hick, P.P., et al., 2004. The Solar Mass Ejection Imager (SMEI) mission. Sol. Phys 225, 177–207.

Jackson, B.V., Hudson, H.S., Nichols, J.D., et al., 1989. Design considerations for a "Solar Mass Ejection Imager" on a rotating spacecraft. Solar System Plasma Physics. In: Waite, Jr., J.H., Burch, J.L., Moore, R.L. (Eds.), Geophysical Monograph, 54, p. 291.

Kelsall, T., Weiland, J.L., Franz, B.A., et al., 1998. The *COBE* diffuse infrared background experiment search for the cosmic infrared background. II. Model of the interplanetary dust cloud. Astrophys. J. 508, 44–73.

Kuchar, T., Buffington, A., Arge, C.N., et al., 2008. Observations of a comet tail disruption induced by the passage of a CME. J. Geophys. Res. 113, A04101, 1–11. doi:10.1029/2007JA012603.

Kwon, S.M., Hong, S.S., Weinberg, J.L., 2004. An observational model of the zodiacal light brightness distribution. New Astron. 10, 91–107.

Leinert, Ch., Bowyer, S., Haikala, L.K., et al., 1998. The 1997 reference of diffuse night sky brightness. Astron. Astrophys. Supp. Ser. 127, 1–99.

Leinert, Ch., Grün, E., 1990. Interplanetary dust, in physics and chemistry in space–space and solar physics. In: Schwenn, R., Marsch, E. (Eds.). Physics of the Inner Heliosphere I, Large-Scale Phenomena, 20. Springer-Verlag.

Leinert, Ch., Pitz, E., 1989. Zodiacal light observed by Helios throughout solar cycle No. 21: Stable dust and varying plasma. Astron. Astrophys. 210, 399–402.

Lumme, K., Bowell, E., 1985. Photometric properties of zodiacal light particles. Icarus 62, 54–71.

Mizuno, D.R., Buffington, A., Cooke, M.P., et al., 2005. Very high-altitude aurora observations with the Solar Mass Ejection Imager. J. Geophys. Res. 110, A07230, 1–18. doi:10.1029/2004JA010689.

Noah, P.V., Noah, M.A., 2001. Validation Report for the Celestial Background Scene Descriptor (CBSD) Zodiacal Emission Model CBZODY6. AFRL-VS-TR-2001-1578. National Technical Information Service, Springfield.

Reach, W.T., 1988. Zodiacal emission. I. Dust near the Earth's orbit. Astrophys. J. 335, 468–485.

Reach, W.T., 1991. Zodiacal emission. II. Dust near ecliptic. Astrophys. J. 369, 529–543.

Spreckley, S.A., Stevens, L.R., 2007. A search for transits and stellar variability in all sky photometry obtained from the solar mass ejection imager. In: Proceedings of Astronomical Society of the Pacific, Conference Series, 'Transiting Extrasolar Planets Workshop', 366, p. 39.

Tappin, S.J., Buffington, A., Cooke, M.P., et al., 2004. Tracking a major interplanetary disturbance with SMEI. Geophys. Res. Lett. 31, L02802, 1–4. doi:10.1029/2003GL018766.

Webb, D.F., Mizuno, D.R., Buffington, A., et al., 2006. Solar Mass Ejection Imager (SMEI) Observations of CMEs in the heliosphere. J. Geophys. Res. 111, A12101, 1–19. doi:10.1029/2006JA011655.